Shock Waves (2010) 20:271–284
DOI 10.1007/s00193-010-0266-y

ORIGINAL ARTICLE

Computation of weak steady shock reflections by means of an unstructured shock-fitting solver

Mikhail S. Ivanov · Aldo Bonfiglioli · Renato Paciorri · Filippo Sabetta

Received: 30 September 2009 / Revised: 14 April 2010 / Accepted: 15 June 2010 / Published online: 3 August 2010

Abstract Weak steady Mach reflections are numerically simulated using unstructured grids by means of either "shock-fitting" or "shock-capturing" techniques. It is shown that shock-fitting allows using coarser meshes than those required by shock-capturing, since the latter needs mesh refinement in the direction normal to the discontinuities, which is not needed using the former approach. The shock-fitted solution is also free from the numerical disturbances that arise along the captured discontinuities and pollute the captured solution in the smooth flowfield region. Finally, the shock-fitting solutions show the presence of a small region next to the Mach stem and the reflected shock downstream of the triple point, characterized by very high gradients.

Communicated by E. Timofeev and H. Kleine.

This paper was based on work that was presented at the 27th International Symposium on Shock Waves, St. Petersburg, Russia, 19–24 July 2009.

M. S. Ivanov
Khristianovich Institute of Theoretical and Applied Mechanics (ITAM), Novosibirsk 630090, Russia
e-mail: ivanov@itam.nsc.ru

A. Bonfiglioli (✉)
Dipartimento di Ingegneria e Fisica dell'Ambiente, Università degli Studi della Basilicata, Viale Ateneo Lucano 10, 85100 Potenza, Italy
e-mail: aldo.bonfiglioli@unibas.it

R. Paciorri · F. Sabetta
Dipartimento di Meccanica ed Aeronautica, Università di Roma, La Sapienza, Via Eudossiana, 18, 00184 Rome, Italy
e-mail: paciorri@dma.dma.uniroma1.it

F. Sabetta
e-mail: sabetta@dma.dma.uniroma1.it

Keywords Steady Mach reflection · Unstructured grids · Shock-fitting · Shock-capturing · Anisotropic mesh adaptation

1 Introduction

The recent introduction of the shock-fitting (S-F) technique within the unstructured grid framework [13] has reopened the development of shock-fitting methodologies, neglected for many years. This novel technique appears to be extremely promising, because it overcomes many of the limitations and difficulties that caused, by the end of 1980s, the dismissal of the shock-fitting techniques in favour of the algorithmically simpler shock-capturing (S-C) techniques. At the same time, it removes by the roots all those numerical issues [4,8] related to capturing gasdynamic discontinuities that have not been completely solved in more than 30 years of developments and efforts [7].

To explore the potential of this new technique, two flows characterized by weak Mach reflection have been considered in this paper. The choice of this kind of flow is dictated by several interesting aspects. The flow is complex enough (three shocks and one contact discontinuity interacting at the triple point) to provide a general assessment of the capabilities and the performances of this novel shock-fitting technique compared to state-of-the-art shock-capturing techniques. At the same time, the weak Mach reflection is a flow configuration which, more than a century after its first observation made by Mach, is still rich of open issues. Among these open issues, it is worth remembering here the one related to the validity of the three-shock theory proposed by von Neumann. Specifically, experiments and numerical tests of weak Mach reflection [2,15] often show a flow behaviour around the triple point that differs from that forecast by the model and

the disagreement between the observed data and the theory is attributed by several authors to the viscosity effects that take place inside the shocks in the proximity of the triple point [2,14].

On the basis of these considerations, numerical simulations of weak Mach reflections performed by means of a shock-fitting technique in the framework of the inviscid (Euler) equations are of particular significance. Indeed, the shock-fitting technique is able to remove completely the effects of the numerical viscosity inside the shocks and to introduce an explicit fitting of the triple point based on von Neumann's three-shock-theory. On the other hand, in a shock-capturing simulation the effects of the numerical viscosity inside the shocks cannot be completely removed and no explicit treatment of the triple point can be introduced.

To enable the computations of these solutions, the shock-fitting algorithm originally presented in [13] has been improved by including the fitting of contact discontinuities and triple points. The paper reports a complete description of this enhanced shock-fitting algorithm and a detailed analysis of the shock-fitting solutions. In order to perform a comparison with more established techniques, the same flow conditions have been computed using a shock-capturing scheme, supplemented with anisotropic mesh adaptation, and these results have been compared with those obtained by means of a shock-fitting scheme.

2 Test case definition

Figure 1 shows a uniform, supersonic stream being deflected through an angle θ_w by the presence of a wedge located on the wall of a straight, planar channel. The oblique shock wave (incident shock, IS) which originates at the concave corner reaches the opposite, straight wall and is reflected by means of a Mach reflection whenever the wedge angle is greater than the maximum deflection angle that the supersonic stream (M_{IS}) behind the incident shock can sustain. The triple point (TP) is the special point where the incident shock interacts with a strong shock, named the Mach stem (MS), that terminates on the straight wall as a normal shock. The interaction between the Mach stem and the incident shock gives rise to a reflected shock (RS) and a contact discontinuity, or slipstream (SS).

Observe from Fig. 1 that an expansion fan also originates at the convex corner where the wedge terminates and the upper wall is deflected through the same angle θ_w, but in the opposite direction, to run again parallel to the opposite wall.

We have considered two flow conditions that were already studied by one of the authors in [2]. The fluid is a monoatomic perfect gas with adiabatic index, $\gamma = 5/3$. The freestream Mach number equals $\mathrm{M}_\infty = 1.7$ in both cases while two different flow deflections θ_w have been considered, as summarized in Table 1. Since the former flow condition had been left un-labelled in [2], we decided to name it case 0.

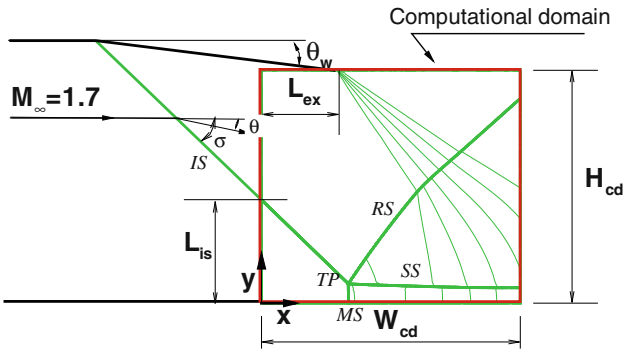

Fig. 1 Mach reflection

For both test cases the computational domain is restricted to a rectangular region having width W_{cd} and height H_{cd}, respectively, equal to 2 and 1.4 dimensionless units (see the red marked box in Fig. 1). Placing the origin of the reference frame in the left bottom corner of the computational domain, L_{ex} denotes the abscissa of the center of the expansion fan and L_{is} is the ordinate of the point where the incident shock enters the computational domain.

Both flow conditions give rise to a Mach reflection which can be analytically solved using von Neumann's three-shock theory. Table 1 gives the flow direction θ_{ss} downstream of the triple point, the shock angle σ[1] and the values of the Mach number downstream of the Mach stem and the reflected shock. The solution at the triple point is easily determined using pressure-deflection diagrams (see Fig. 2a, b) which refer to both flow conditions under consideration. The intersection between the shock polars of the incident shock and reflected shock gives the (equal) pressure and deflection of the flow at the triple point downstream of the Mach stem and reflected shock. Observe that in both cases the reflected shock and the Mach stem are strong shocks, hence the downstream flow is subsonic. The difference between these two flow conditions lies in the fact that in case 0 the reflected shock deflects the flow towards the (horizontal) freestream direction, whereas in case 2 the reflected shock deviates the flow farther away from the freestream direction. These two different configurations are classified as standard and non-standard Mach reflections in [1]. The different behaviour can also be seen from the shock polars. In case 0, depicted in Fig. 2a, the angle formed by the slipstream is smaller than that imposed by the wedge $\theta_{\mathrm{SS}} < \theta_w$, whereas the opposite is true in case 2, as shown in Fig. 2b. This seemingly minor difference between the two test cases however gives rise to flowfields that display different and peculiar characteristics, particularly in the neighbourhood of the triple point.

[1] Measured with respect to the direction of the upstream flow.

Table 1 Testcase definition

Case	θ_w	L_{ex}	L_{is}	θ_{SS}	M_{IS}	σ_{IS}	p_2/p_1	M_{RS}	σ_{RS}	M_{MS}	σ_{MS}	p_{3-4}/p_1
0	8.5°	1	0.8	7.2754°	1.3389	46.6061°	1.6574	0.7780	87.5170°	0.6899	81.9985°	3.2925
2	12°	0.6	1.2	14.1384°	1.1639	53.1841°	2.0653	0.9008	79.8978°	0.8521	68.4047°	2.8731

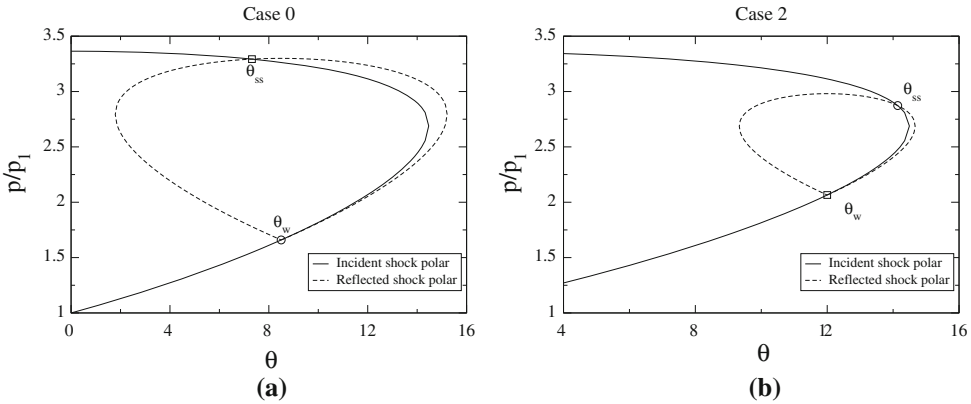

Fig. 2 Pressure-deflection diagrams corresponding to the flow cases of Table 1. **a** *Case 0* $\theta_w = 8.5°$, **b** *Case 2* $\theta_w = 12°$

3 Numerical procedures

The two flow conditions described in Sect. 2 have been simulated using two different unstructured-grid approaches based on the numerical solution of the Euler equations, written in conservation-law-form. In what follows, we shall refer to these two approaches as: shock-capturing and shock-fitting. Both employ the same shock-capturing solver within the smooth, i.e. discontinuity-free, regions of the flowfield, whereas they differ for the treatment of discontinuities, both shocks and slip-lines. The shock-capturing approach is standard: all discontinuities are computed just like any other region of the flowfield and feature a finite (grid-dependent) thickness with one or more grid-points located in between the upstream and downstream states. In order to improve the spatial resolution in the neighbourhood of the discontinuities, an anisotropic mesh refinement technique [5,6] is used in conjunction with the shock-capturing approach.

The second approach uses a shock-fitting technique to explicitly track the motion of shocks and sliplines, whereas the smooth regions of the flow-field are computed using the same spatial discretization adopted in the shock-capturing approach. Since the shock-fitting algorithm is a new development, it will be described in full length in Sect. 3.2.

3.1 Shock-capturing solver

Since both numerical approaches rely on the same CFD solver it is worth briefly describing its main features. EulFS is a shock-capturing code which employs fluctuation splitting (or residual distribution) schemes for the spatial discretization. Introduced in the early 1980s by Roe, fluctuation splitting schemes have features of both Finite Volume and Finite Element methods. The data representation is bi-linear in space and continuous across the element interfaces. The spatial discretization is applied to a preconditioned version of the Euler equations, which relies on the preconditioning matrix proposed by van Leer et al. [16]. The reason for using preconditioning for these high speed flows lies in the fact that it allows to preserve total enthalpy across steady captured shocks. A more detailed description of the unstructured CFD solver can be found in [3].

3.2 Shock fitting algorithm

In a recent paper [13], a floating shock-fitting technique, inspired by the original work of Moretti and Abbett [9], has been implemented in conjunction with the unstructured CFD solver described in Sect. 3.1. In this novel unstructured shock-fitting approach the shock front is discretized as a polygonal curve which is treated as an internal boundary by the CFD solver. The local shock speed and nodal values on the high pressure side of the shock are computed by enforcing the Rankine–Hugoniot relations across the discontinuity. The shock is allowed to move over and independently of a background triangular grid which is locally adapted at each time step to ensure that the nodes and the edges that make up the shock are part of a constrained Delaunay triangulation that covers the entire computational domain.

In the present paper, two new features have been added to the methodology described in [13]: (1) not only shocks, but also contact discontinuities are fitted and (2) the triple point is modelled using von Neumann's three-shock theory.

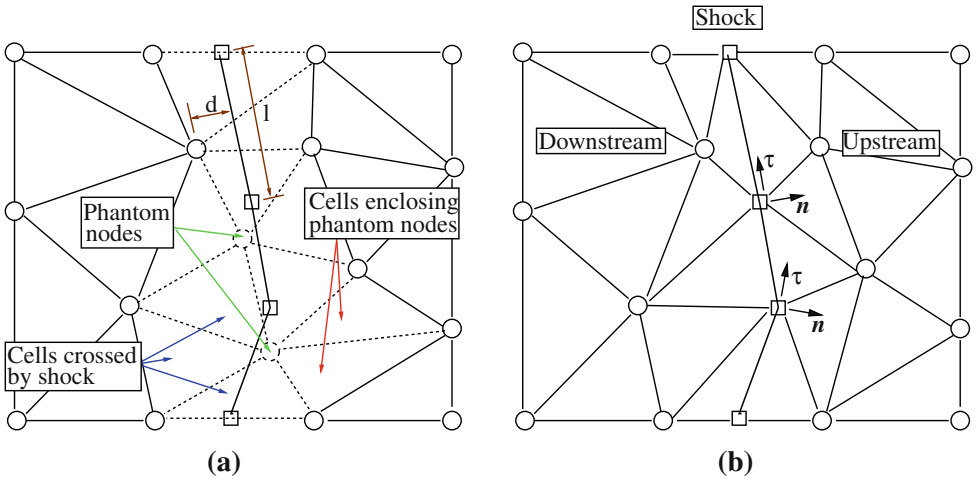

Fig. 3 Local re-meshing in the neighbourhood of the fitted discontinuity. **a** Cell removal, **b** local constrained Delaunay triangulation

Let us consider a two-dimensional domain and a shock front crossing this domain at time level t (see Fig. 3a). In what follows we shall describe the case of a shock wave, but most of the algorithmic features to be described in the following sections apply to contact discontinuities as well. Whenever needed, a distinction will be made between the case of a shock and that of a contact discontinuity.

The shock front is shown in bold by a polyline whose endpoints are the shock points, marked by squares. A background triangular mesh, whose nodes are denoted by circles, covers the entire computational domain and the position of the shock points is completely independent of the location of the nodes of the background grid. While each node of the background mesh is characterized by a single set of state variables, two sets of values, corresponding to the upstream and downstream states, are assigned to each shock point.

We assume that at time t the solution is known at all grid and shock points. The computation of the flow field at the subsequent time level $t + \Delta t$ can be split into several steps that will be described in detail in the following sub-sections.

3.2.1 Cell removal around the discontinuity

The first step consists of removing those cells of the background mesh that are crossed by the discontinuity, along with the mesh points which are located too close to the shock front. These nodes are declared as "phantom" nodes and all cells having at least one phantom node among their vertices are also removed from the background triangulation (see the dashed circles and cells in Fig. 3a).

3.2.2 Local re-meshing around the shock front

Following the cell removal step, the remaining part of the background mesh is split into two regions separated by a hole containing the shock. This hole is then re-meshed using a constrained Delaunay triangulation: both the shock segments and the edges belonging to the boundary of the hole are constrained to be part of the final triangulation, as shown in Fig. 3b. No further mesh point is added during this triangulation process. Upon completion of this stage, the computational domain is discretized by a modified mesh in which the shock points and the shock edges are part of the triangulation. In this modified mesh, which differs from the background mesh only in the neighbourhood of the fitted fronts, each discontinuity behaves like an interior boundary and divides the computational domain into two non-communicating sub-domains, see Fig. 4. This is achieved by replacing each shock point by two superimposed mesh points: one belonging to the downstream region and the other to the upstream region. Downstream and upstream states are correspondingly assigned to each pair of shock nodes. In the following sections, we shall use the subscripts u and d to denote the upstream and downstream state for the gridpoints belonging to the fitted discontinuities.

3.2.3 Computation of the tangent and normal unit vectors

The tangent $\boldsymbol{\tau}$ and normal $\mathbf{n}$ unit vectors have to be computed at each point along the discontinuities since this is required to properly apply the jump relations, as described in Sect. 3.2.5. The computation of these vectors for a generic shock point, see Fig. 3b, is carried out using finite-difference formulae (see [13] for further details) which involve the coordinates of the shock point itself and those of the neighbouring shock points that belong to its domain of dependence. Specifically, centered finite difference formulae are used when the downstream state is subsonic whereas upwind formulae are employed whenever the downstream state is supersonic. The unit vector $\mathbf{n}$ is conventionally assumed to be directed from the high entropy (downstream) towards the low entropy (upstream) side of the discontinuity.

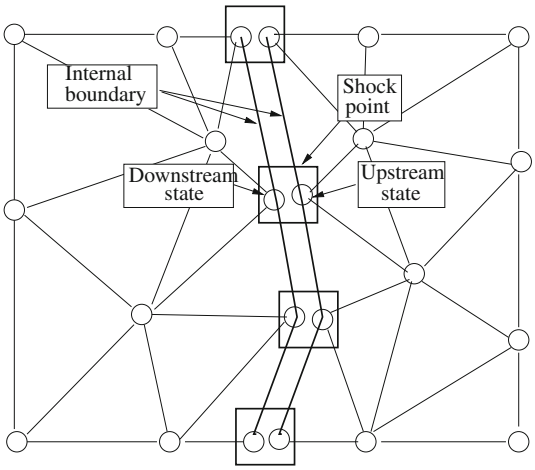

Fig. 4 The shock is treated as an internal boundary

It is also convenient to express the components of the velocity vector in the $(\mathbf{n}, \boldsymbol{\tau})$ reference frame of each discontinuity point:

$$u_n = \mathbf{u} \cdot \mathbf{n} \quad u_\tau = \mathbf{u} \cdot \boldsymbol{\tau}$$

3.2.4 Solution update using the capturing code

Using the modified mesh as input, a single time step calculation is performed using the unstructured CFD solver which provides updated nodal values within all grid and shock points at time level $t + \Delta t$. Since the discontinuities are seen by the CFD code as internal boundaries where no boundary condition is imposed, the solution for the mesh points located on the upstream and downstream sides of a discontinuity will be updated using information coming only from the computational sub-domain which is attached to that side of the discontinuity. This has different consequences, depending on whether the discontinuity is a shock or a slip-line and whether the gridpoint belongs to the upstream or downstream side of the discontinuity.

If we consider the upstream state of a shock wave, the update provided by the CFD solver at time level $t + \Delta t$ is entirely correct. Indeed, within the supersonic, upstream (low-pressure) region, all waves (acoustic, entropy and vorticity) propagate towards the shock so that no boundary condition is required on this internal boundary. The situation is different within the subsonic region attached to the downstream (high-pressure) side of the shock. Here the entropy, vorticity and forward moving acoustic wave propagate away from the discontinuity. Therefore, the provisional values computed by the CFD code for the gridpoints located on the downstream side of the shock are wrong, since three (in two spatial dimensions) boundary conditions, corresponding to the aforementioned waves, are missing on the shock-downstream internal boundary. The downstream region is however subsonic and the backward moving acoustic wave propagates the following signal:

$$R_d^{t+\Delta t} = \tilde{a}_d^{t+\Delta t} + \frac{\gamma - 1}{2} (\tilde{u}_n)_d^{t+\Delta t}, \tag{1}$$

from the downstream region towards the downstream side of the shock. Due to the upwind nature of the spatial discretization, one can, therefore, assume that the Riemann variable defined by Eq. (1) is correctly computed by the CFD code.

In Eq. (1), $\tilde{a}_d^{t+\Delta t}$ and $\tilde{\mathbf{u}}_d^{t+\Delta t}$ are the values of the acoustic and flow velocity of the downstream state of the shock nodes computed by the CFD solver. These flow variables have been marked with a "tilde" to emphasize the fact that these are the provisional (incorrect) values computed at time $t + \Delta t$ by the CFD code before enforcing the jump relation across the discontinuity, as described in Sect. 3.2.5.

If a contact discontinuity is considered instead, both the upstream and downstream states are in general incorrect except for the following set of characteristic variables:

$$R_d^{t+\Delta t} = \tilde{a}_d^{t+\Delta t} + \frac{\gamma - 1}{2} (\tilde{u}_n)_d^{t+\Delta t} \tag{2a}$$

$$R_u^{t+\Delta t} = \tilde{a}_u^{t+\Delta t} - \frac{\gamma - 1}{2} (\tilde{u}_n)_u^{t+\Delta t} \tag{2b}$$

$$S_d^{t+\Delta t} = \frac{\tilde{p}_d^{t+\Delta t}}{(\tilde{\rho}_d^{t+\Delta t})^\gamma} \tag{2c}$$

$$S_u^{t+\Delta t} = \frac{\tilde{p}_u^{t+\Delta t}}{(\tilde{\rho}_u^{t+\Delta t})^\gamma} \tag{2d}$$

$$(u_\tau)_d^{t+\Delta t} = (\tilde{u}_\tau)_d^{t+\Delta t} \tag{2e}$$

$$(u_\tau)_u^{t+\Delta t} = (\tilde{u}_\tau)_u^{t+\Delta t} \tag{2f}$$

since these are associated with acoustic, entropy and vorticity waves that do not cross the boundary and, therefore, their correct evolution does not require any exchange of information across the contact discontinuity.

3.2.5 Enforcement of the jump relations

The missing pieces of information that are needed to correctly update the solution within all gridpoints located on the discontinuities are provided in the current step, which consists in enforcing the Rankine-Hugoniot relations between the upstream and downstream states. A different treatment is required for shocks and contact discontinuities.

Let us first consider a shock point. For notational convenience, we now introduce the flow velocity relative to the discontinuity:

$$\mathbf{v} = \mathbf{u} - \mathbf{w} \tag{3}$$

where $\mathbf{w}$ is the velocity of the discontinuity relative to an inertial reference frame. As explained in Sect. 3.2.4, the shock

upstream state ($\mathbf{u}_u, a_u, \rho_u$) has been correctly updated at time level $t + \Delta t$ by the CFD solver. At the downstream state only the Riemann variable $R_d^{t+\Delta t}$ is correctly computed by the CFD solver.

The "correct" downstream state and the shock speed component w_n normal to the discontinuity are then obtained by solving a system of five non-linear algebraic equations. Four of these are the Rankine–Hugoniot jump relations:

$$\rho_u^{t+\Delta t}\,(v_n)_u^{t+\Delta t} = \rho_d^{t+\Delta t}\,(v_n)_d^{t+\Delta t} \tag{4a}$$

$$p_u^{t+\Delta t} + \rho_u^{t+\Delta t}\left(v_n^2\right)_u^{t+\Delta t} = p_d^{t+\Delta t} + \rho_d^{t+\Delta t}\left(v_n^2\right)_d^{t+\Delta t} \tag{4b}$$

$$(u_\tau)_u^{t+\Delta t} = (u_\tau)_d^{t+\Delta t} \tag{4c}$$

$$H_u^{t+\Delta t} = H_d^{t+\Delta t} \tag{4d}$$

$$R_d^{t+\Delta t} = a_d^{t+\Delta t} + \frac{\gamma - 1}{2}\,(u_n)_d^{t+\Delta t} \tag{4e}$$

while the fifth equation uses the only "correct" information, given by Eq. (1), computed by the CFD solver on the downstream side of the shock. In Eqs. (4), H is the specific total enthalpy of the relative motion:

$$H = \frac{\gamma}{\gamma - 1}\frac{p}{\rho} + \frac{v_n^2 + v_t^2}{2}.$$

Observe that all variables in the RHS of Eqs. (4) are unknown, whereas all values on the LHS (except the shock speed w_n) are those "correctly" updated by the CFD solver at time level $t + \Delta t$. The five unknown quantities are $a_d^{t+\Delta t}$, $\rho_d^{t+\Delta t}$, the two cartesian components of the velocity vector $\mathbf{u}_u^{t+\Delta t}$ and the shock speed $w_n^{t+\Delta t}$, since pressure can be expressed as a function of sound speed and density. A Newton–Raphson algorithm is used to solve the system of Eqs. (4) within each shock point.

Similarly to a shock point, a gridpoint belonging to a contact discontinuity is characterized by two states and by the velocity of the discontinuity along the normal to the front (w_{cd}). There are nine unknowns in total: the velocity components, density and pressure on both sides and the velocity of the discontinuity. All these variables can be updated at time level $t + \Delta t$ by solving an algebraic system of non-linear equations which comprises the jump relations for the contact discontinuity:

$$p_u^{t+\Delta t} - p_d^{t+\Delta t} = 0 \tag{5a}$$

$$(u_n)_u^{t+\Delta t} - w_{cd}^{t+\Delta t} = 0 \tag{5b}$$

$$(u_n)_d^{t+\Delta t} - w_{cd}^{t+\Delta t} = 0 \tag{5c}$$

and the six "characteristic" equations already given in Eqs. (2).

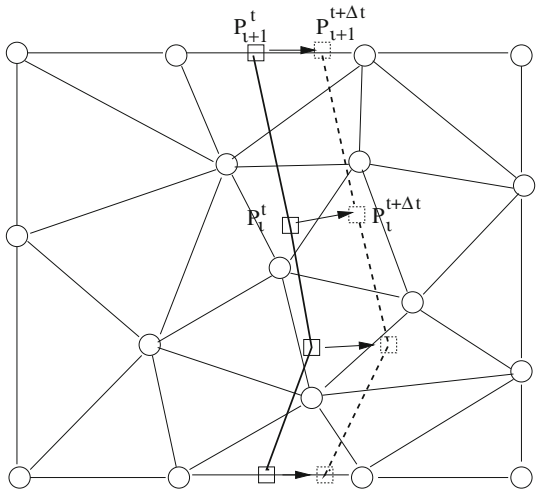

Fig. 5 Shock displacement

3.2.6 Shock displacement

As shown in Fig. 5, the new position of the shock front at time $t + \Delta t$ is obtained by displacing all shock points using the following first order integration formula:

$$P^{t+\Delta t} = P^t + w^{t+\Delta t}\mathbf{n}\Delta t. \tag{6}$$

The low temporal accuracy of this formula does not affect the spatial accuracy of the steady-state solutions, which only depends upon the spatial accuracy of the gasdynamic solver and of the tangent and normal vector computation.

3.2.7 Triple point treatment

Whenever two or more discontinuities interact, the fitting algorithm described in Sect. 3.2.5 for isolated shocks or sliplines breaks down and an ad-hoc procedure has to be devised to model the interaction point in which discontinuities meet. Different types of interactions can be observed in real-life situations, such as those between shocks of the same or different family. In this section we shall describe the numerical treatment of the triple point which arises in Mach reflections.

Figure 6 sketches the flowfield in the neighbourhood of the triple point: the triple point velocity vector $\mathbf{w}^{TP}$ is shown along with the nomenclature used in this section.

Let us start by assuming that at time t a modified mesh is available in which the triple point, the shocks and the contact discontinuity are part of the triangulation (see Fig. 7). In this modified mesh the presence of the triple point splits the computational domain into four non-communicating regions each of which is bounded by a pair of discontinuities which meet at the triple point. These regions have been numbered from one to four in Fig. 7: freestream conditions have been labelled with 1, 2 denotes the flow state behind the incident

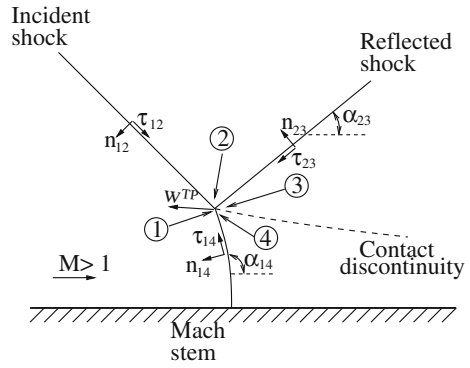

Fig. 6 Schematic representation of a Mach reflection in the neighbourhood of the triple point

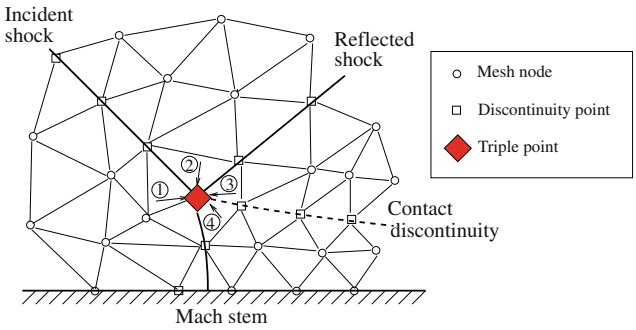

Fig. 7 Mesh in the proximity of the triple point

shock; 3 is the region behind the reflected shock and 4 is the region downstream of the Mach stem.

As mentioned in Sect. 3.2, all points located on a shock or slip line are characterized by two sets of state variables, corresponding to the upstream and downstream states. On the other hand, four different flow states are assigned to the triple point, each corresponding to the four regions shown in Fig. 7.

We begin the description of the triple point fitting procedure by noting that the computation of the normal and tangent unit vectors at the triple point according to the procedure described in Sect. 3.2.3 can be carried out without violating the domain of dependence only for the incident shock. This is because the flow downstream of the incident shock is supersonic so that the $\mathbf{n}$ and $\boldsymbol{\tau}$ unit vectors along the incident shock can be computed using upwind finite difference formulae that involve the coordinates of the triple point itself and those of other shock points that are located along the incident shock, ahead of the triple point. On the other hand, the same computing procedure can neither be applied to the reflected shock, regardless of whether the flow downstream of it is supersonic or subsonic, nor to the Mach stem, whose downstream flow is always subsonic. In both cases, indeed, the use of centered (in the case of subsonic flow) or upwind (in the case of supersonic flow) finite difference formulae would require the use of shock points located outside the endpoints of the reflected shock and Mach stem. These observations highlight the fact that the slopes of the Mach stem and reflected shock at the triple point should be taken as unknowns. In practice, we use as unknown quantity the angle α, formed by the shock and the flow direction in the uniform region 1, and denote as α_{23} and α_{14} the slopes of the reflected shock and that of the Mach stem at the triple point. Observe that the normal and tangent unit vectors can be conveniently expressed in terms of the angle α:

$$\mathbf{n} = (\sin\alpha; -\cos\alpha)^T \quad \boldsymbol{\tau} = (\cos\alpha; \sin\alpha)^T.$$

When the CFD code updates the solution at time level $t + \Delta t$ within each of the four regions surrounding the triple point, all four states associated with the triple point change. However, only the state 1 is "correctly" updated to time $t + \Delta t$, for the same reason explained in Sect. 3.2.4, whereas the other three states have not been correctly updated and, therefore, have to be re-computed by enforcing the jump relations at the triple point. In summary, the unknowns of the triple point problem are the states 2, 3 and 4 at time $t + \Delta t$ (12 unknowns), the slope of the reflected shock and that of the Mach stem (2 unknowns) and the triple point velocity vector (2 unknown components) for a total number of 16 unknowns. As far as the triple point velocity vector is concerned, the components associated with the basis $(\mathbf{n}_{12}, \boldsymbol{\tau}_{12})$:

$$\left(w^{\mathrm{TP}}_{n_{12}}\right) = \mathbf{w}^{\mathrm{TP}} \cdot \mathbf{n}_{12} \quad \left(w^{\mathrm{TP}}_{\tau_{12}}\right) = \mathbf{w}^{\mathrm{TP}} \cdot \boldsymbol{\tau}_{12}$$

will be used as unknowns.

The calculation of these 16 unknown quantities can be split into two sub-problems. Indeed, state 2 can be computed using the shock point calculation described in Sect. 3.2.5 by taking the states 1 and 2, respectively, as upstream and downstream and by setting $\mathbf{n} = \mathbf{n}_{12}$. This is easily understood if one considers that the flow state downstream of the incident shock only depends upon the freestream condition and the flow deflection enforced by the presence of the wedge. The shock speed obtained by the solution of this sub-problem is the triple point velocity component in the direction normal to the incident shock: $w^{\mathrm{TP}}_{n_{12}}$.

The remaining eleven unknowns are computed by solving a system of as many non-linear algebraic equations. Eight of these are the four Rankine–Hugoniot relations (4) written for both the reflected shock and the Mach stem.

In all these eight jump relations, the normal component of the shock speed is a function of the triple point velocity vector $\mathbf{w}^{\mathrm{TP}}$, since the three shocks cannot move independently, but their motion is coupled through that of the triple point:

$$\mathbf{w}^{\mathrm{TP}} = w^{\mathrm{TP}}_{n_{12}}\mathbf{n}_{12} + w^{\mathrm{TP}}_{\tau_{12}}\boldsymbol{\tau}_{12} \tag{7a}$$

$$= w^{\mathrm{TP}}_{n_{23}}\mathbf{n}_{23} + w^{\mathrm{TP}}_{\tau_{23}}\boldsymbol{\tau}_{23} \tag{7b}$$

$$= w^{\mathrm{TP}}_{n_{14}}\mathbf{n}_{14} + w^{\mathrm{TP}}_{\tau_{14}}\boldsymbol{\tau}_{14} \tag{7c}$$

The normal components $w_{n_{23}}^{\mathrm{TP}}$ and $w_{n_{14}}^{\mathrm{TP}}$ are those that enter the jump relations for the reflected shock and Mach stem, respectively. These normal components can be expressed as a function of the unknown tangential velocity component of the incident shock $w_{\tau_{12}}^{\mathrm{TP}}$ at the triple point and the unknown slopes of the reflected shock (α_{23}) and Mach stem (α_{14}):

$$w_{n_{ij}}^{\mathrm{TP}} = w_{n_{12}}^{\mathrm{TP}} \left(\sin\alpha_{12}\sin\alpha_{ij} + \cos\alpha_{12}\cos\alpha_{ij}\right) + w_{\tau_{12}}^{\mathrm{TP}} \left(\cos\alpha_{12}\sin\alpha_{ij} - \sin\alpha_{12}\cos\alpha_{ij}\right) \quad (8)$$

The system is closed by von Neumann's relations for the slipstream:

$$p_4 - p_3 = 0 \quad (9a)$$

$$|\mathbf{u}_4 \times \mathbf{u}_3| = 0 \quad (9b)$$

and by the Riemann variable associated with the upstream moving acoustic wave of region 4:

$$a_4^{t+\Delta t} + \frac{\gamma - 1}{2} u_{n_{14}}^{t+\Delta t} = R_4^{t+\Delta t} \quad (10)$$

which is correctly evolved by the CFD solver.

4 Comparative analysis of the results

As mentioned previously, the two test cases described in Sect. 3 have been computed by means of two approaches that differ considerably in the treatment of shocks and contact discontinuities. It is therefore appropriate to compare the computational aspects of both approaches while describing the results that have been obtained.

4.1 Test case 0

Both computing approaches start from the same solution obtained by the shock-capturing solver on a baseline, unadapted mesh. Figure 8a shows a detail of the this grid along with the corresponding shock-capturing numerical solution, which is displayed in Fig. 8b. This baseline mesh has been generated using a frontal-Delaunay algorithm [10,11] and is almost entirely made of equilateral triangles. The mesh pattern is clearly visible in the computed Mach number contour lines which display a meandering shape along the Mach stem and a staircase effect along the reflected shock. All shocks are also characterized by a relatively large numerical thickness, since this isotropic grid features the same mesh spacing across the discontinuities as well as in the smooth regions of the flowfield. Figure 8b shows the strong, detrimental effects due to the misalignment between the cell edges and the shock front which gives rise to spurious disturbances causing the wiggly behaviour of the Mach number isolines downstream of the Mach stem.

The first row of Table 2 reports the number of nodes and triangles of the baseline mesh along with the normalized maximum and minimum cell area and their ratio. These geometric features are supplemented with those displayed in Fig. 9, which shows along the ordinates the percentage number of cells that meet the geometric features plotted along the abscissae: the aspect ratio in Fig. 9a and minimum and maximum angles in Fig. 9b. Although various definitions of the aspect ratio may be given, we have used the ratio of inscribed circle radius to circumcircle radius, normalized so that the aspect ratio takes value 1 for an equilateral triangle and 0 for a degenerate triangle.

Concerning the baseline mesh, all geometric indicators confirm that it is made of equilateral triangles, which is certainly a convenient triangular shape in smooth regions of the flowfield, but, when used across the discontinuities, gives rise to the un-physical shock shapes noted previously.

The shock-capturing solution obtained on the baseline mesh is fed to the ANGENER [5] anisotropic mesh generator to obtain a refined mesh in which cells are clustered in regions of high gradients and coarsened elsewhere. This refined mesh allows the computation of a new shock-capturing solution that can be used as input for an additional mesh-refinement step. In order to improve the spatial resolution of the shock-capturing solution, the refinement and solution steps are iterated several times until the adapted mesh shows no significant changes in topology and number of cells between two successive iterations. For the present cases, six or seven grid levels were found to be sufficient to obtain a nearly grid-converged solution.

Figure 8c shows an enlargement around the triple point region of the last grid level obtained using the anisotropic mesh refinement algorithm; the corresponding shock-capturing solution is displayed in Fig. 8d. The comparison between Fig. 8a, b shows the significant changes produced by the anisotropic mesh refinement algorithm on the computational mesh.

First of all, the total number of cells in the anisotropically refined mesh has increased by a factor of five with respect to that of the baseline mesh, since grid refinement in the neighbourhood of the discontinuities is only partially balanced by mesh coarsening in smooth regions. Second, the anisotropic mesh refinement algorithm has reduced the mesh size in the direction normal to the discontinuities, thus giving rise to triangular cells that are highly elongated in the direction tangential to the discontinuities. Indeed, Fig. 9a shows that the triangles in the anisotropically refined mesh uniformly cover the entire range of aspect ratios. The distribution of the minimum and maximum angles (shown in Fig. 9b) suggests that most of these triangles feature an angle close to 90°.

The effect of the anisotropic mesh refinement upon the computed solutions can be observed by comparing Fig. 8b, d. The numerical thickness of the shocks has been remarkably

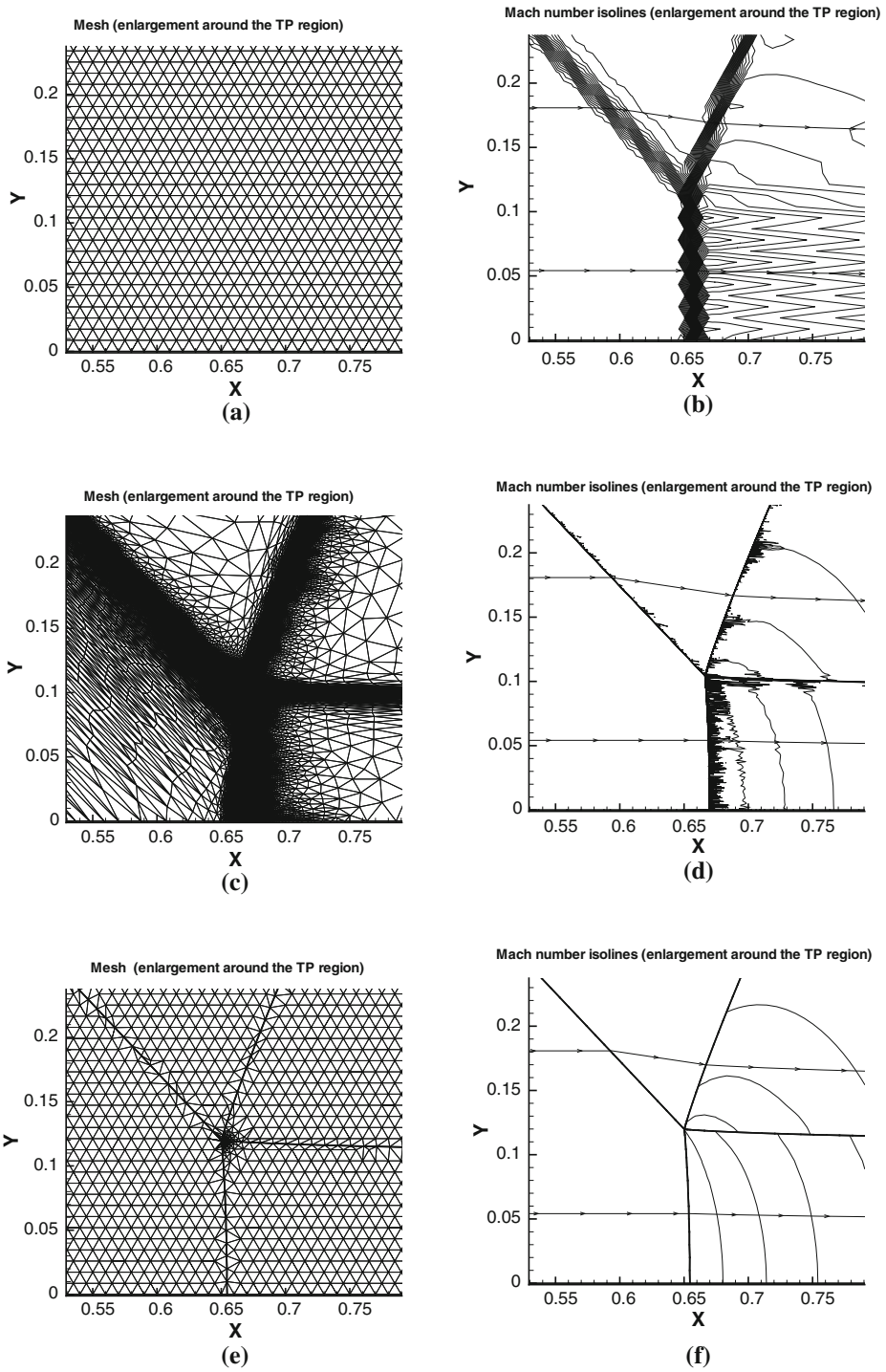

Fig. 8 Case 0: comparison between the shock-capturing and shock-fitting solutions. **a** Baseline mesh, **b** shock-capturing solution computed on the baseline mesh, **c** anisotropically refined mesh, **d** shock-capturing solution computed on the anisotropically refined mesh, **e** modified shock-fitting grid, **f** shock-fitting solution computed on the modified mesh

Table 2 Geometric parameters of the various meshes used for case 0

	No. of nodes	No. of triangles	$A_{\min}/(W_{cd}H_{cd})$	$A_{\max}/(W_{cd}H_{cd})$	$A_{\max}/A_{\min}$
Baseline mesh	32,588	64,495	8.93×10^{-6}	2.21×10^{-5}	2.5
Last level of the anisotropic mesh	161,036	321,554	9.43×10^{-10}	2.29×10^{-3}	$2.4 \times 10^{+6}$
Modified mesh used in the shock-fitting approach	35,588	65,062	3.64×10^{-12}	2.31×10^{-5}	$6.3 \times 10^{+6}$

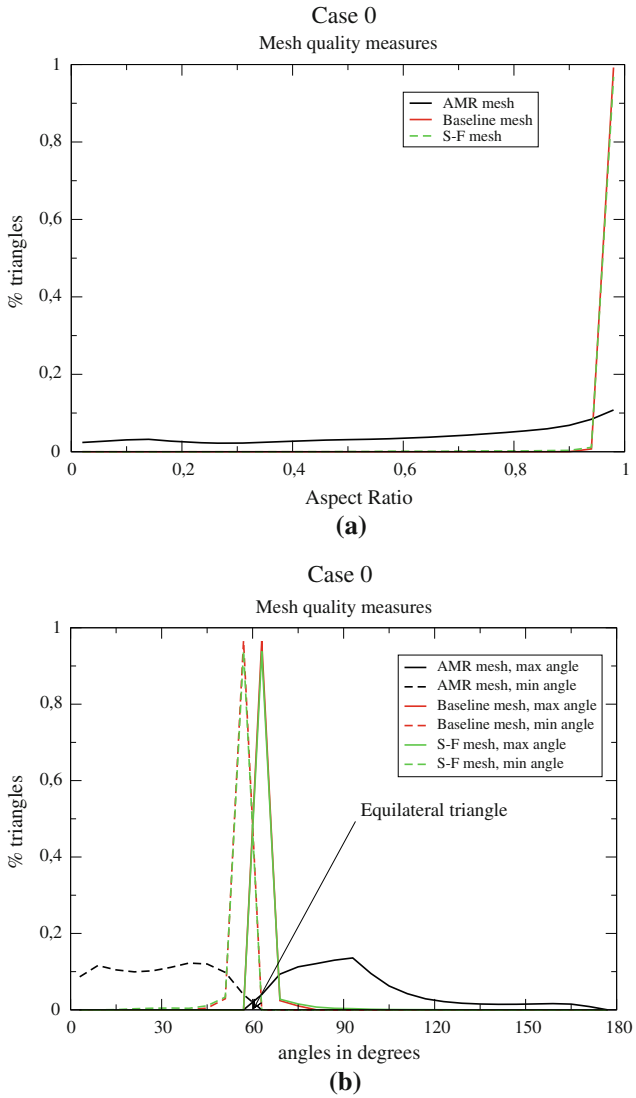

Fig. 9 Geometric characteristics of the three grids used for case 0. **a** Aspect ratio, **b** min and max angles

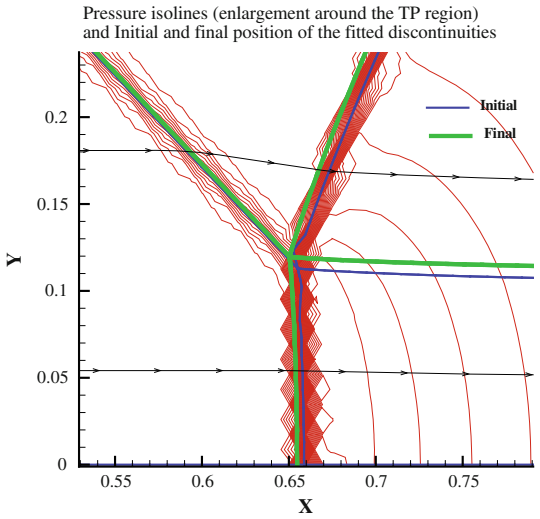

Fig. 10 Shock-fitting simulation: initial and final positions of the fitted discontinuities

reduced, since gridpoints have been clustered in the shock normal direction. Moreover, since anisotropic mesh refinement has given rise to elongated triangles featuring two edges almost aligned with the shock front, the disturbances originating along the discontinuities have been considerably reduced with respect to what we had previously observed on the baseline grid. Nevertheless, Fig. 8d shows that non-negligible disturbances are still generated even on the adapted mesh not only by the Mach stem, but also by the reflected shock and slipstream.

A general remark concerning the solution-driven adaptation used in the shock-capturing calculation is that the reduction in cell size produced by the anisotropic mesh refinement algorithm is primarily driven by the high gradients that occur in the direction normal to the discontinuities.

We now turn our attention to the shock-fitting approach. Since no shock detection mechanism is currently implemented in the shock-fitting algorithm, the simulation needs to be initialized using the shock-capturing solution. This is used to provide an approximate estimate of the initial position of the shocks, slipstream and triple point which is needed to construct the internal boundaries corresponding to the various discontinuities. The isotropic, baseline mesh is used as the background triangulation for the shock-fitting algorithm, apart from a local modification in the neighbourhood of the triple point which shall be described next. Starting from this initial flow-field, the solution is integrated in time according to the algorithm illustrated in Sect. 3.2 until reaching the steady state.

Figure 10 shows a detailed view of the pressure isolines in the neighbourhood of the triple point: the initial and final position of the shocks and slipstream computed by means of the shock-fitting algorithm have been superimposed onto the shock-capturing solution computed on the baseline mesh.

Figure 8e displays the steady-state, modified mesh generated by the shock-fitting algorithm and Fig. 8f shows corresponding solution. It is worth emphasizing that this mesh is very similar to the background (baseline) one except in the regions surrounding the discontinuities and the triple point where it has been locally modified to accommodate the gridpoints and edges that belong to the shocks and contact discontinuity. Moreover, since the flow is characterized by the presence of a small region near the triple point, downstream of the Mach stem and reflected shock, where the gradients are very high, the mesh has been further refined in this region to ensure sufficient spatial resolution. To satisfy this requirement, the gridpoints located along the Mach stem, reflected shock and slipstream have been clustered near the

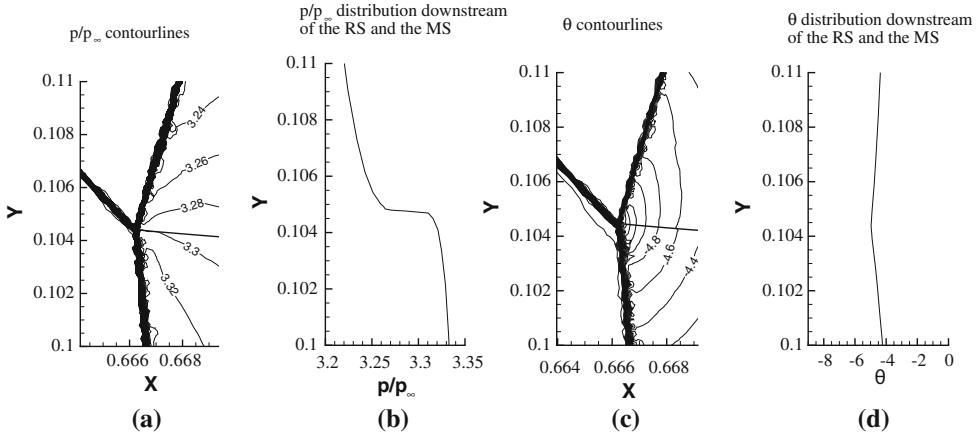

Fig. 11 Case 0: shock-capturing solution computed on the last grid level of the anisotropically refined mesh

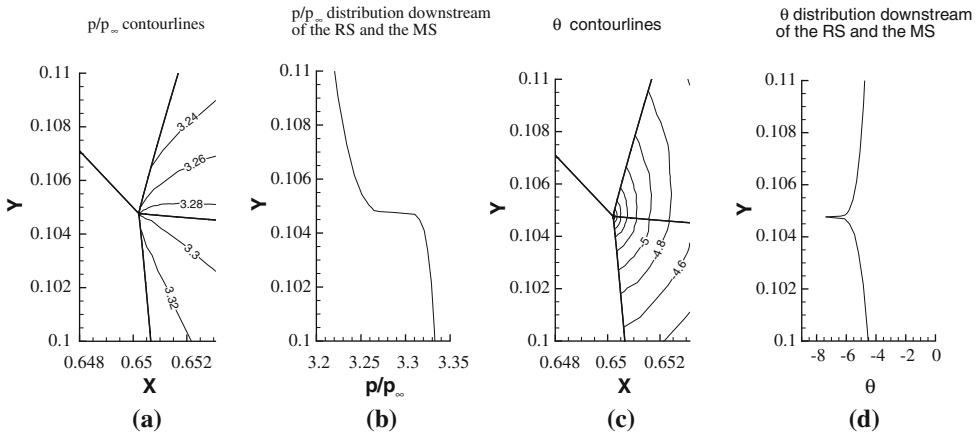

Fig. 12 Case 0: shock-fitting solution computed on the modified mesh

triple point and, in addition to this, several tens of gridpoints have been added to the background triangulation within the smooth regions surrounding the triple point. This local grid clustering can be seen in Fig. 8e.

The Mach number iso-contours computed using the shock-fitting technique are displayed in Fig. 8f. The solution is neat and does not display any spurious disturbances that characterize the shock-capturing solutions previously analyzed.

The analysis of the geometric parameters of the modified shock-fitting mesh (see the third row of Table 2) suggests further comments. The number of cells and nodes of this mesh is only slightly larger than that of the baseline mesh. The minimum cell area is two orders of magnitude smaller than that observed in the anisotropically refined mesh, but the distribution of the aspect ratio is almost superimposed to that of the baseline mesh. Indeed, the local mesh refinement in the shock-fitting simulation is only driven by the solution gradients computed within the smooth regions and, contrary to the shock-capturing approach, it is not needed across the discontinuities. For this reason, the local mesh refinement required in the neighbourhood of the triple point is achieved in the shock-fitting simulation with only a modest increase in the overall number of cells and without introducing highly elongated triangles.

Let us now focus our attention towards the immediate neighbourhood of the triple point. Figures 11 and 12 display the normalized pressure (p/p_1) field and the flow deflection angle θ. The one-dimensional distribution of these quantities (plotted against y) along the downstream side of the reflected shock and Mach stem is shown in Fig. 11b, d for shock-capturing and in Fig. 12b, d for shock-fitting. Observe that the pressure distribution displays a steep gradient at the triple point whereas the flow deflection shows a cusp at the same location.

This behaviour is clearly resolved in the shock-fitting solution, whereas it is somewhat blurred in the corresponding shock-capturing solutions. This is seen by comparing Fig. 11b with 12b for the pressure field and Fig. 11d with 12d for the deflection angle. This behaviour can be explained by the fact that the shock-capturing solution is characterized by a mesh spacing in the triple point region which is coarser than that used in the shock-fitting calculation, despite the fact that the anisotropically refined mesh has by far many more cells and gridpoints than the shock-fitting

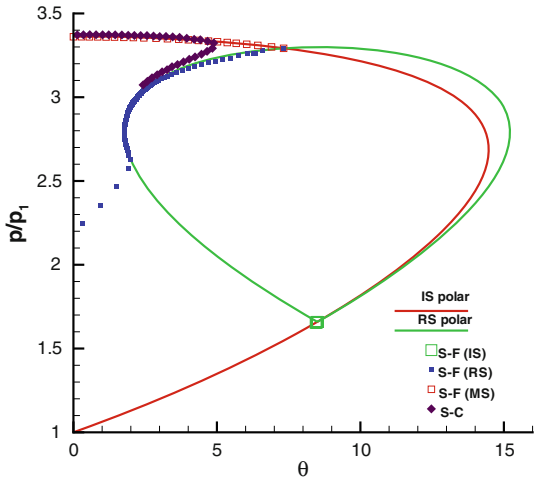

Fig. 13 Case 0: shock polars

mesh. This observation is confirmed by the pressure-deflection diagram of Fig. 13, where the analytical shock polars have been compared with the numerical states extracted from the shock-fitting and shock-capturing solutions along the downstream side of the Mach stem and reflected shock. The low spatial resolution of the shock-capturing solution causes a significant departure of the numerical results from the analytical curves that are well fitted by the shock-fitting solution.

Indeed, a correct computation with the shock-capturing approach would require a spatial resolution in the triple point region at least as fine as that used in the shock-fitting approach, but this area of fine mesh spacing would extend to a wider region, because the mesh must ensure not only a good resolution in the downstream region where high gradients occur, but also a numerical shock thickness much smaller than the size of the downstream region. This last requirement is not necessary in the shock-fitting approach because the fitted shocks are treated as true discontinuities having zero thickness.

4.2 Test case 2

The second Mach reflection considered in this paper appears to be more severe than the first one and, for this reason, it better allows us to demonstrate the capabilities and the potential of the proposed shock-fitting technique.

Similarly to the previous case, a shock-capturing solution, computed on an isotropic baseline mesh, is used as starting point for the anisotropic mesh refinement procedure used in conjunction with the shock-capturing simulation. This baseline mesh and the corresponding shock-capturing solution have also been used to initialize the shock-fitting simulation.

Table 3 summarizes the geometric characteristics of three different meshes: the baseline and the last grid level of the anisotropically refined mesh used in the shock-capturing calculations and the modified mesh used in the shock-fitting approach.

Comparing the data reported in Table 3 with those of case 0 (see Table 2), one sees that the number of gridpoints and cells has increased with respect to the previous case for both approaches. However, the increase amounts to 13.5% for the shock-capturing simulation and to only about 0.1% for the shock-fitting one.

An overall view (not reported here) of the entire computational domain shows that the isolines of the shock-fitting and the shock-capturing solutions on the anisotropically refined mesh are nearly superimposed. Significant differences are, however, observed between the two solutions if the comparison is restricted to a narrow region centered around the triple point. The following analysis will therefore concentrate on the neighbourhood of the triple point.

The non-dimensional pressure field is displayed in Figs. 14a and 15a for the shock-capturing and shock-fitting solutions, respectively. Similarly, Figs. 14c and 15c display the iso-contours of the flow deflection angle.

First of all one sees that the iso-contours computed by means of shock-fitting are free from the disturbances that characterize the corresponding shock-capturing solutions.

Similarly to case 0, the shock-fitting solution clearly shows the presence of a small region on the downstream side of the Mach stem and the reflected shock characterized by very high gradients. These gradients appear to be even stronger than those observed in the previous case, as can be inferred by observing the one-dimensional distributions of the normalized pressure (respectively, flow angle) that are plotted along the downstream side of the Mach stem and reflected shock in Fig. 15b, d. It is worth observing that also the pressure distribution is characterized by the presence of a narrow cusp at the triple point, whereas in case 0 only the flow deflection showed such a behaviour.

The comparison between Figs. 14a and 15a shows that the numerical thickness of the captured shocks is very large compared to the size of the region downstream of the triple point where the high gradients occur. This observation points to the insufficient mesh resolution of the anisotropically refined mesh in that region (despite the large overall number of gridpoints and cells), but also to an intrinsic difficulty for a solution-based adaptation criterion to discriminate between gradients across a captured discontinuity and those that may eventually arise just downstream of it.

Lack of resolution in the shock-capturing solution is clearly seen when looking at the distributions of pressure and flow angle extracted immediately downstream of the Mach stem and reflected shock. Both quantities are different from those predicted by the shock-fitting simulation: compare Fig. 14b with 15b and Fig. 14d with 15d. There exists, however, a qualitative resemblance between the flow angle

Table 3 Geometric parameters of the various meshes used for case 2

	No. of nodes	No. of triangles	$A_{\min}/(W_{cd}H_{cd})$	$A_{\max}/(W_{cd}H_{cd})$	$A_{\max}/A_{\min}$
Baseline mesh	32,618	64,556	5.96×10^{-6}	4.46×10^{-5}	7.5
Last grid level of the anisotropic mesh	184,340	368,180	8.46×10^{-10}	2.39×10^{-3}	$2.8 \times 10^{+6}$
Modified mesh used in the shock-fitting approach	35,618	65,156	3.06×10^{-12}	2.35×10^{-5}	$7.7 \times 10^{+6}$

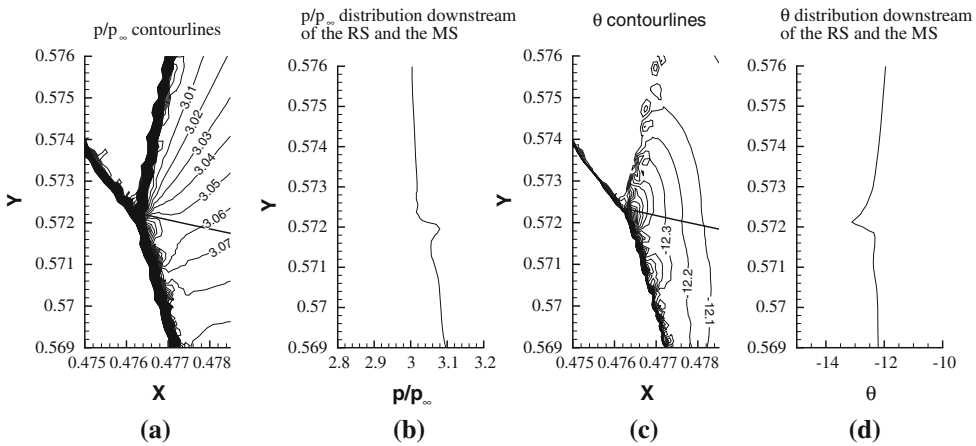

Fig. 14 Case 2: shock-capturing solution computed on the last grid level of the anisotropically refined mesh

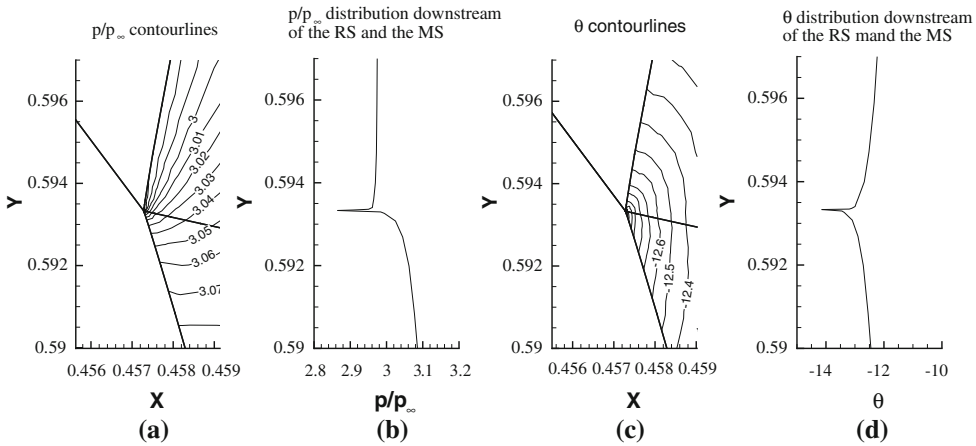

Fig. 15 Case 2: shock-fitting solution computed on the modified mesh

distributions, whereas the pressure distributions differ completely, both qualitatively and quantitatively.

The pressure-deflection diagram shown in Fig. 16, which is built using the downstream states along the Mach stem and reflected shock, confirms the previous observations and proves the correctness of the results obtained using the shock-fitting approach. Indeed, the shock-fitting solution (red and blue symbols in Fig. 16) closely follows the analytical curves up to the triple point, which is the point of intersection between the incident shock and the reflected shock polars. In contrast to this, the shock-capturing solution (diamonds in Fig. 16) initially follows the reflected shock polar along the Mach stem, but then abandons the reflected shock polar and joins the incident shock polar without ever reaching the triple point.

It is important to stress that the differences between the shock-capturing and the shock-fitting solutions are significant only within a small neighbourhood of the triple point. Zooming away from it, good agreement is recovered between the two solutions.

5 Conclusions

The unstructured shock-fitting technique described in the present paper has been successfully applied to the simulation of steady weak Mach reflections. The results obtained using this newly developed technique have been compared with those obtained using a more conventional shock-capturing technique, supplemented with anisotropic mesh adaptation.

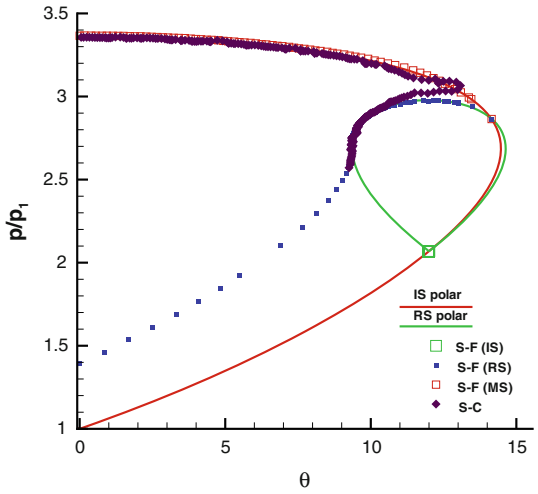

Fig. 16 Case 2: shock polars

The shock-fitting simulations show that the Euler solution of weak Mach reflections is characterized by a small region, located downstream of the triple point and bordered by the Mach stem and the reflected shock, where high streamwise and crossflow gradients occur. A correct computation of this region imposes an extremely fine mesh resolution. The shock-fitting technique was able to satisfy these mesh requirements without a significant increase in the overall number of gridpoints and cells. On the other hand, the shock-capturing approach used in this study, despite a remarkable increase in the number of mesh cells produced by the mesh refinement procedure, was not able to adequately resolve this special flow region.

It is our opinion that beyond the specific shock-capturing solver and mesh-refinement technique used in this paper, at least for this class of problems, the shock-capturing solutions may not achieve the same quality as that obtained using the shock-fitting approach. Indeed, in a shock-capturing solution the gradients across the shock are not well distinguishable from those that may eventually occur within the regions immediately downstream of the shock. Moreover, as the mesh resolution of a shock-capturing simulation is increased, the gradient across the shock tends artificially towards infinity, whereas the gradients outside the shock converge towards finite values. The behaviour of a shock-capturing solution in the limit of vanishing mesh size does represent a remarkable challenge for any a-posteriori mesh adaptation procedure. Indeed, since solution-based mesh refinement depends upon the numerical evaluation of local derivatives of the flow variables, gradients computed inside a captured shock tend to hide those evaluated in the immediate neighbourhood of the shock. As a consequence, the application of a mesh refinement procedure to a shock-capturing solution cannot ensure adequate mesh resolution in flow regions, such as those surrounding triple points, where strong, but finite gradients occur.

In the shock-fitting approach this does not occur because shocks and slip-lines are modelled as true discontinuities and do not need any kind of mesh refinement in the direction normal to the discontinuity.

Acknowledgments Authors wish to express their gratitude to M.D. Salas for his valuable comments and suggestions concerning the shock-fitting algorithm and M. Grottadaurea for checking the manuscript. The mesh quality statistics displayed in Fig. 9 have been computed using the GRUMMP [12] software. Financial support from MIUR under Grant PRIN-2007 is gratefully acknowledged.

References

1. Ben-Dor, G.: Shock Wave Reflection Phenomena. Springer, Berlin (2007)
2. Bondar, Y., Khotyanovsky, D., Kudryavtsev, A., Shoev, G., Ivanov, M.: Viscosity effects on Mach reflection in steady flows. In: 46th AIAA Aerospace Sciences Meeting and Exhibit, AIAA 2008-4257. American Institute of Aeronautics and Astronautics, Reston (2008)
3. Bonfiglioli, A.: Fluctuation splitting schemes for the compressible and incompressible euler and Navier–Stokes equations. Int. J. Comput. Fluid Dyn. **14**(1), 21–39 (2000)
4. Carpenter, M.H., Casper, J.H.: Accuracy of shock capturing in two spatial dimensions. AIAA J. **37**(9), 1072–1079 (1999)
5. Dolejsi, V.: ANGENER, version 3.1. http://www.karlin.mff.cuni.cz/~dolejsi/angen/angen3.1.htm
6. Dolejsi, V.: Anisotropic mesh adaptation for finite volume and finite element methods on triangular meshes. Comput. Vis. Sci. **1**(3), 165–178 (1998)
7. Moretti, G.: Thirty-six years of shock fitting. Comput. Fluids **31**(5), 719–723 (2002)
8. Lee, T.K., Zhong, X.: Spurious numerical oscillations in simulation of supersonic flows using shock-capturing schemes. AIAA J. **37**(3), 313–319 (1999)
9. Moretti, G., Abbett, M.: A time-dependent computational method for blunt body flows. AIAA J. **4**(12), 2136–2141 (1966)
10. Müller, J.D.: DELAUNDO. http://www.cerfacs.fr/~muller/delaundo.html
11. Müller, J.D., Roe, P., Deconinck, H.: A frontal approach for internal node generation in Delaunay triangulations. Int. J. Numer. Methods Fluids **17**, 241–256 (1993)
12. Ollivier-Gooch, C.: GRUMMP–generation and refinement of unstructured, mixed-element meshes in parallel. http://tetra.mech.ubc.ca/GRUMMP/
13. Paciorri, R., Bonfiglioli, A.: A shock-fitting technique for 2D unstructured grids. Comput. Fluids **38**(3), 715–726 (2009)
14. Sternberg, J.: Triple-shock-wave interactions. Phys. Fluids **2**(2), 179–206 (1959)
15. Szwaba, R., Doerffer, P., Namiesnik, K., Szulc, O.: Flow structure in the region of three shock wave interaction. Aerosp. Sci. Technol. **8**(6), 499–508 (2004)
16. van Leer, B., Lee, W.T., Roe, P.: Characteristic time-stepping or local preconditioning of the Euler equations. In: AIAA 10th Computational Fluid Dynamics Conference. AIAA-91-1552-CP (1991)